


## Control of a spectral minimum in high-order harmonic generation by adjusting the phase-matching conditions in a gas medium

Zhiming Yin,<sup>1</sup> Xiangyu Tang,<sup>1</sup> Chi Zhang ,<sup>1</sup> Yong Fu,<sup>1</sup> Jiaxin Han,<sup>1</sup> Jiahao You,<sup>1</sup> Beiyu Wang,<sup>1</sup> and Cheng Jin <sup>1,2,\*</sup>

<sup>1</sup>Department of Applied Physics, *Nanjing University of Science and Technology*, Nanjing, Jiangsu 210094, China

<sup>2</sup>MIT Key Laboratory of Semiconductor Microstructure and Quantum Sensing,

Engineering Research Center of Semiconductor Device Optoelectronic Hybrid Integration in Jiangsu Province, *Nanjing University of Science and Technology*, Nanjing, Jiangsu 210094, China



(Received 7 May 2024; accepted 25 July 2024; published 16 August 2024)

A spectral minimum in the high-order harmonic generation (HHG) is of great interest, usually generated by specific atoms or molecules. Here we show through detailed simulations that the minimum in the HHG spectrum can be created and tuned by varying the phase-matching conditions when a gas medium is located at the focus of a long-wavelength laser. We reveal that the minimum can be shifted spatially depending on the quantum orbit due to its sensitivity to the phase-matching condition. We provide a formula to relate the position of the minimum to the coherence length of HHG. We also show that the position(s) and the number of (multiple) minimum(s) can be changed by varying the beam waist and the intensity of the driving laser. In addition, we establish the scaling relations with the laser wavelength to maintain the spectral position of the minimum. We expect that this method can be effectively implemented to shape the attosecond pulse in the extreme ultraviolet and soft x rays.

DOI: [10.1103/PhysRevA.110.023107](https://doi.org/10.1103/PhysRevA.110.023107)

### I. INTRODUCTION

High-order harmonic generation (HHG) is a well-known nonlinear phenomenon when an intense femtosecond laser interacts with a gas medium [1–7]. The typical spectral distribution of HHG emission includes three parts: rapid decrease at the lower orders, a plateau region with gentle intensity change, and a cutoff region with sharply decreasing intensity. Due to its unique and wide plateau, the spectral range of HHG can be extended to the extreme ultraviolet (XUV) and soft x rays [8–11], making it a favorable light source for synthesizing attosecond pulses [12,13]. With the ultrashort time resolution provided by such pulse, it is possible to control and detect electron dynamics in matter [14–22]. Due to its good coherence in space and time, HHG has also been widely used in other fields, such as molecular-orbital tomography [23], HHG spectroscopy [24], and nanoscale structure imaging [25].

The issue of generating a minimum in the HHG spectrum has been of great interest, extensively investigated in a number of experimental and theoretical studies. For example, in some applications, such as multispectral spectrometry [26], element-specific coherent imaging [27], and photoionization or photoemission experiments [28], the spectral structure of the generated HHG spectrum is desirable to be modified, which can be achieved by using the minimum in its spectrum. Recently, the minimum in the HHG spectrum has been used to shape attosecond pulses [29–32]. Such shaped pulse adds an additional degree of controlling the electron dynamics. For example, Fu *et al.* [33] showed that the laser-dressed lineshape of Fano resonance can be rapidly modified within the timescale of tens of attoseconds if the atomic system

is excited by a double-peaked attosecond pulse. There are several different ways to create the minimum in the HHG spectrum. According to an extended version of the well-known three-step model [34], the HHG spectrum contains the information about the electronic structure of an atomic target, imprinted through the photoionization cross section (PICS). Thus one can generate the minimum in the HHG spectrum, inheriting from the minimum in the PICS. A typical example is the “Cooper minimum” in the PICS of Ar, which has been observed in the HHG spectra in many experiments [35–41]. If molecules are transiently aligned by a femtosecond laser under a nonadiabatic scheme, the minimum can also be generated in the HHG spectrum. Here we take the CO<sub>2</sub> molecule as an example [42–51]. Two types of the minimum exist. One is called the “structural” minimum [42,43], which originates from the minimum of the PICS at each fixed alignment angle, but its position and depth could be changed by coherently averaging over the alignment distribution. The other one is called the “dynamical” minimum [44,45], due to interference between the highest occupied molecular orbital (HOMO) and the inner orbitals (such as HOMO-1, HOMO-2, and so on) in the HHG process. Its position can be varied by changing the intensity of the HHG driving laser. Jin and Lin [52] also showed that the two-color laser pulse can be used to generate a shallow minimum in the HHG spectrum of Ne under some specific phase-matching conditions. Very recently, Li *et al.* [32] proposed a quasi-phase-matching scheme of using two gas jets to create and control the minimum in the HHG spectrum. They were able to shift the position of the minimum in the XUV by adjusting the distance between two jets when the gas pressure is properly chosen. All approaches above have their own limitations. It is desirable to develop other simple and easy-operated methods to produce and tune the minimum in the HHG spectrum of atoms.

\*Contact author: [cjin@njust.edu.cn](mailto:cjin@njust.edu.cn)

It is well known that the generation process of HHG in the gas medium can be divided into two steps [53,54]. The first one is the interaction of the atom and the local laser field, called as the single-atom response, which can be accurately computed by solving the time-dependent Schrödinger equation (TDSE). The second one is the macroscopic response, including the coherent summation of harmonic emissions from each atom in the gas medium, which can be well taken into account by solving the Maxwell's wave equations of the driving laser and the generated high-harmonic field. This step is also generally described by using the term of "phase matching." Since the phase-matching conditions of HHG are very sensitive to the macroscopic parameters, such as the laser focusing geometry, the gas-jet position, the pulse energy, and so on, they could be used to control the structure of the HHG spectrum. Is it possible to create the minimum in the HHG spectrum by adjusting the phase-matching conditions just with a single-color driving laser? Note that this scheme is relatively easy to perform experimentally.

In this article, our main goal is to offer a feasible method to tune the minimum generated in the HHG spectrum of atoms with the single-color laser. We analyze how the quantum orbits and the phase-matching conditions influence the harmonic minimum by using the well-established HHG theory of macroscopic propagation. Our method is based on using the unfavorable phase-matching condition, usually avoided in the generation of the HHG. To the best of our knowledge, this method has not been presented by others in the literature. This paper is organized as follows: In Sec. II, we present the theoretical methods for simulating single-atom HHG, macroscopic propagation of HHG in the gas medium, and far-field harmonic emissions. In Sec. III, we present HHG results with the minimum after macroscopic propagation, analyze the phase-matching conditions of high harmonics in the near field, explain the formation of the harmonic spatial profile in the far field, and tune the position(s) and the number of the harmonic (multiple) minimum(s). The conclusions are given in Sec. IV.

## II. THEORETICAL METHODS

### A. Single-atom high-order harmonic generation response

The strong-field approximation (SFA) model proposed by Lewenstein *et al.* [55] has been widely used to simulate the single-atom response. However, there exists the difference between high harmonics computed by the SFA and by solving the TDSE. To solve this problem, the Lin's group introduced the quantitative rescattering (QRS) model [56–58], which aims to compute the single-atom harmonic spectrum as accurate as the TDSE. In the SFA model, harmonic emissions from different quantum paths can be separated using the saddle-point approximation. This is also known as the quantum orbit (QO) model [56,59–62]. The QO model can also be modified in the frame of the QRS model. The QRS model has been validated by comparing its results with those obtained by the TDSE as well as experimental measurements [63]. Note that all the computed results of the single-atom response in this paper are obtained using the QRS model.

### 1. Lewenstein (or strong-field approximation) model

According to the Lewenstein model under the strong-field approximation [55,64], the time-dependent induced dipole moment can be written in the form of the following integral:

$$x(t) = -i \int_{-\infty}^t dt' \left( \frac{-2\pi i}{t-t'-i\epsilon} \right)^{3/2} d_x^*(p_s + A(t)) \times d_x(p_s + A(t')) E(t') e^{-iS(p_s, t, t')} + \text{c.c.}, \quad (1)$$

where  $E(t)$  is the applied laser field, and  $A(t)$  is the vector potential. They can be related in the following:

$$A(t) = - \int_{-\infty}^t dt''' E(t'''). \quad (2)$$

$p_s$  is the saddle-point solution for momentum, which is given by

$$p_s = - \frac{1}{t-t'} \int_{t'}^t A(t'') dt'', \quad (3)$$

and  $S(p_s, t, t')$  is the classical action of the electron during propagation in the electric field, which is expressed as

$$S(p_s, t, t') = \int_{t'}^t dt'' \left( \frac{1}{2} [p_s + A(t'')]^2 + I_p \right). \quad (4)$$

Here  $I_p$  is the ionization potential of the target, and  $t'$  and  $t$  are the ionization and recombination moments of the electron, respectively. Note that in Eq. (1), one can truncate the excursion time of the electron to select contribution to the single-atom HHG (or the electron wave packet) from different electron returns.

For hydrogenlike atoms, the dipole matrix element describing the transition from the ground state to the continuum (or the plane-wave state) is given by

$$d(p) = \langle p | \hat{d} | g \rangle = i \left( \frac{2^{7/2} (2I_p)^{5/4}}{\pi} \right) \frac{p}{(p^2 + 2I_p)^3}. \quad (5)$$

### 2. Quantum orbit model

Applying the saddle-point approximation, the following two equations can be obtained for the harmonic with the angular frequency  $\omega$  [56,59–62]:

$$\frac{1}{2} [p_s + A(t')]^2 = -I_p, \quad (6)$$

and

$$\frac{1}{2} [p_s + A(t)]^2 = \omega - I_p. \quad (7)$$

Here the first equation corresponds to the quantum effect of tunneling ionization of the electron, and the second equation represents emission of the photon with the energy  $\omega$  by recombination of the electron with the parent ion.

The induced-dipole moment in the frequency domain can be expressed as

$$x(\omega) = \sum_s \frac{2\pi}{\sqrt{\det(S'')}} \left( \frac{-2\pi i}{t_s - t'_s} \right)^{3/2} d_x^*(p_s + A(t_s)) \times d_x(p_s + A(t'_s)) E(t'_s) e^{-i\Theta(p_s, t, t'_s)}, \quad (8)$$

where each pair  $(t_s, t'_s)$  determines a unique quantum orbit represented by  $s$ , the phase factor  $\Theta(p_s, t, t') = S(p_s, t, t') - \omega t$ ,

and the calculation of the determinant  $\det(S'')$  is straightforward. In Eq. (8), one can select contribution to the single-atom HHG (or the electron wave packet) either from one specific quantum orbit or from multiple quantum orbits.

### 3. Quantitative rescattering model

In the QRS model [56–58], the induced-dipole moment of an atomic target under a linearly polarized laser can be written as

$$x(\omega) = W(\omega)d(\omega), \quad (9)$$

where  $d(\omega)$  is the complex photorecombination (PR) transition dipole matrix element, which reflects the properties of the target, and  $W(\omega)$  is the complex microscopic wave packet, which is mostly determined by the laser.

In the QRS model,  $d(\omega)$  can be precisely calculated by solving the time-independent Schrödinger equation under the single-active electron (SAE) approximation, in which the interaction between the electron and the atomic ion is described by a model potential [65]. In the SFA,  $d^{\text{SFA}}(\omega)$  is obtained by assuming that the continuum state of the ionized electron is a plane wave as shown in Eq. (5), which is not accurate. Meanwhile, the wave packet  $W(\omega)$  in the QRS model is the same as that in the SFA model, and it can be calculated by using the Lewenstein model or the quantum orbit model as

$$W(\omega) = \frac{x^{\text{SFA}}(\omega)}{d^{\text{SFA}}(\omega)}, \quad (10)$$

or

$$W(\omega) = \frac{x^{\text{QO}}(\omega)}{d^{\text{SFA}}(\omega)}. \quad (11)$$

Here  $x^{\text{SFA}}(\omega)$  and  $x^{\text{QO}}(\omega)$  are complex induced-dipole moments, and  $d^{\text{SFA}}(\omega)$  is a pure imaginary or a pure real number.

### B. Propagation equations of the high-harmonic field

We assume that the laser beam is not affected when it is propagated in a macroscopic gas medium. By employing a moving coordinate frame ( $z' = z$  and  $t' = t - z/c$ ) and applying the paraxial approximation, the Maxwell's wave equations for the high-harmonic field in the frequency domain are [41,53,54,64]

$$\nabla_{\perp}^2 \tilde{E}_h(r, z', \omega) - \frac{2i\omega}{c} \frac{\partial \tilde{E}_h(r, z', \omega)}{\partial z'} = -\mu_0 \omega^2 \tilde{P}_{nl}(r, z', \omega), \quad (12)$$

where

$$\tilde{E}_h(r, z', \omega) = \hat{F}[E_h(r, z', t')], \quad (13)$$

$$\tilde{P}_{nl}(r, z', \omega) = \hat{F}[P_{nl}(r, z', t')], \quad (14)$$

and

$$P_{nl}(r, z', t') = [n_0 - n_e(r, z', t')]x(r, z', t'). \quad (15)$$

Here  $\hat{F}$  is the Fourier transform operator acting on the temporal coordinate,  $P_{nl}(r, z', t')$  is the nonlinear polarization,  $n_0$  is the neutral atom density, and  $n_e(r, z', t')$  is the free electron density.  $x(r, z', t')$  is the induced-dipole moment in the time domain obtained with a local laser field at the spatial position

$(r, z')$ , and it can be related to  $x(\omega)$  by the Fourier transform. Once Eq. (12) is solved, the harmonic field  $\tilde{E}_h(r, z', \omega)$  at the exit face of the gas medium is called the near-field harmonic.

### C. Far-field harmonic emission

When the high harmonics are emitted from the exit of the gas medium, they further propagate in vacuum until reaching the spectrometer, referred to as far field. Such propagation process from the near field to the far field can be quantitatively described by using Huygens integral under the paraxial and Fresnel approximations. The high harmonic in the far field is computed by the near-field harmonic in the following:

$$\begin{aligned} E_h^f(r_f, z_f, \omega) &= ik \int \frac{\tilde{E}_h(r, z', \omega)}{z_f - z'} J_0\left(\frac{kr r_f}{z_f - z'}\right) \exp\left[\frac{-ik(r^2 + r_f^2)}{2(z_f - z')}\right] \\ &\quad \times r dr, \end{aligned} \quad (16)$$

where  $J_0$  is the zero-order Bessel function of the first kind,  $z_f$  and  $z'$  are the far-field and near-field positions from the laser focus, respectively,  $r_f$  is the transverse coordinate in the far field.

## III. RESULTS AND DISCUSSION

### A. Generation of the minimum in the high-order harmonic generation spectrum after macroscopic propagation

In the simulations, the temporal electric field of the laser pulse takes the form

$$E(t) = E_0 \cos^2\left(\frac{\pi t}{\tau}\right) \cos(\omega_0 t + \varphi). \quad (17)$$

Here  $E_0$  is the amplitude of the peak laser field,  $\tau$  is the total duration, which is 2.75 times the full-width-at-half-maximum (FWHM) duration of the laser pulse,  $\omega_0$  is the angular frequency, and  $\varphi$  is the carrier-envelope phase (CEP). We choose that the total duration is 30 optical cycles, the wavelength is 1600 nm, and the CEP is fixed at zero. The gas target is chosen as neon atom, whose single-atom HHG spectrum has no minimum. We assume that the incident laser is a Gaussian beam, and its intensity at the laser focus is  $1.5 \times 10^{14}$  W/cm<sup>2</sup> and its beam waist is chosen as 90  $\mu$ m. The gas jet with the length of 1 mm is located at the laser focus. Under these macroscopic parameters, a minimum indeed appears in the HHG spectrum after propagation, which is about centered in the spectrum. Note that we are limited to the low-pressure condition in this work. We have confirmed that such conditions require the gas pressure to be below 10 torr, at which the self-absorption of high harmonics can be safely neglected.

We first show the spectral intensity distributions of HHG in the near field and in the far field in Figs. 1(a) and 1(b), respectively. A clear minimum can be identified in two figures, with the more pronounced minimum structure in the far field. The position of the minimum varies with the radial distance or the divergence angle, exhibiting a curved minimum structure in the intensity distribution. We integrate the harmonic intensity in the far field within two specific ranges of 0–1 mrad and 1.5–2.5 mrad. The resulting harmonic spectra are illustrated

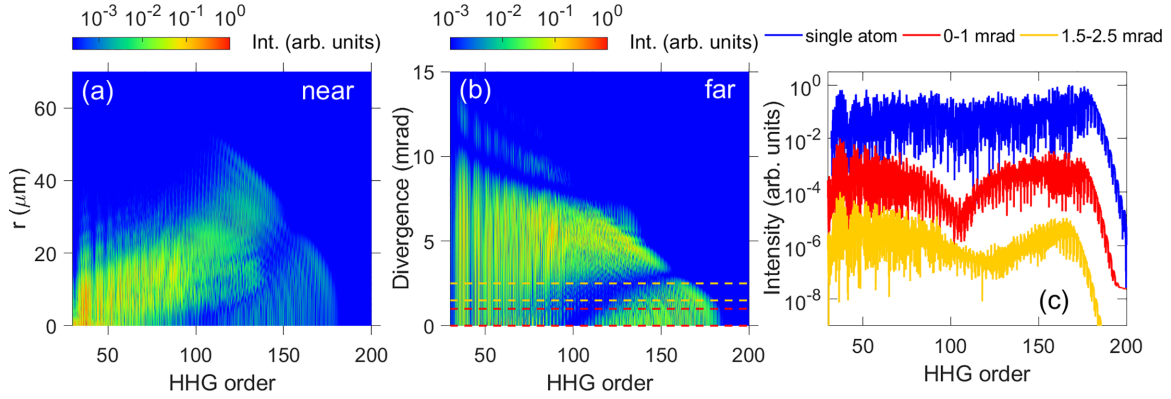


FIG. 1. Harmonic intensity distributions in the (a) near field and (b) far field. “Int.” in the label of the color bar means intensity. (c) Far-field harmonic spectra spatially integrated within 0–1 mrad (red line) and 1.5–2.5 mrad (orange line). Single-atom harmonic spectrum (blue line) is also shown in panel (c) for comparison. The driving laser has a wavelength of 1600 nm, a beam waist of 90  $\mu\text{m}$ , and a peak intensity of  $1.5 \times 10^{14}$  W/cm<sup>2</sup> at the focus. A 1-mm-long Ne gas jet is put at the laser focus.

in Fig. 1(c), clearly showing that the position of the minimum shifts to the higher order with increasing the divergence angle. We also show the single-atom HHG spectrum of Ne in Fig. 1(c) for comparison. There is no minimum in the HHG spectrum because no minimum exists in the PR cross section of the Ne atom [54,66]. Thus appearance of the minimum in the macroscopic HHG spectra is solely due to propagation effects in the gas medium. This is different from the minimum occurring in the HHG spectra of Ar atoms [35–41] and carbon dioxide molecules [42–51]. Note that we have confirmed that the minimum structure presented in Fig. 1 remains unchanged when the SFA is used to compute the single-atom induced dipole moments in the macroscopic HHG simulation. This is because the properties of harmonic emissions from different electron trajectories are solely determined by the microscopic wave packet in Eq. (9), which does not vary from the QRS model to the SFA. Thus, the phase-matching condition of high harmonics also remains the same.

In general, the phase-matching conditions of HHG from different quantum orbits are different. We thus analyze whether the generation of the harmonic minimum depends on the quantum orbit. In Fig. 2, we show the spatial intensity distributions of HHG from different quantum orbits. Here we choose the following quantum orbits: the short orbit of the first return (S1), the long orbit of the first return (L1), the short orbit of the third return (S3), and the long orbit of the third return (L3). The results of the second return are not presented because the cutoff energies of generated HHG spectra are too small to reach the harmonic minimum. In the near field, the position of the minimum does not change along the radial direction (labeled by the red square) for S1 in Fig. 2(a), and the minimum always occurs near the 101th harmonic order (H101) within the spatial range of 0–20  $\mu\text{m}$ . Meanwhile, the minimum is clearly presented for L1, but its position is shifted to the higher order with increasing the radial distance (see red and black circles) in Fig. 2(b). For S3 and L3 in Figs. 2(c) and 2(d), the minimum becomes shallow (or fuzzy), and the general behavior is similar to that for L1. Note that the unclear minimum displaying in the near-field intensity distribution in Fig. 1(a) is because of overlap of harmonic emissions from the quantum orbits of the first and the third returns. In the

far field, harmonic emissions from S1 are only located on axis with a minimum at H101, see Fig. 2(e). For L1, S3, and L3, the minimum clearly displays both on axis and off axis, showing a curved structure in the spatial intensity distribution, see Figs. 2(f)–2(h). For different quantum orbits, we integrate the harmonic intensity in the spatial range of 0–1 mrad. The resulting harmonic spectra are shown in Figs. 2(i)–2(l). It clearly shows that the position of the minimum is not varied with the quantum orbit. Thus, in Fig. 1(b), the minimum appearing on the axis in the far field is due to all quantum orbits, and the off-axis minimum is caused by the quantum orbits longer than the short one in the first return.

## B. Analysis of phase-matching conditions of near-field harmonics from different quantum orbits

### 1. Spatial evolution of harmonic emissions from different quantum orbits in the gas medium

We next try to understand the results from different quantum orbits in the near field in Fig. 2. We plot spatial distributions of the harmonic intensity inside the gas medium for three selected harmonic orders in Fig. 3. Results are shown for different quantum orbits. In the first row, for H61, harmonic emissions from S1 are mostly distributed close to the axis in Fig. 3(a), and we can identify the coherence length  $L_{\text{coh}}$  from the peak intensity along the propagation distance. It is about 0.8 mm. This value decreases with the harmonic order. As labeled in Figs. 2(e) and 2(i),  $L_{\text{coh}}$  is 0.5 mm for H101, and 0.4 mm for H131. In the second row, the radial region of harmonic emissions from L1 is expanded with the harmonic order, as shown by red lines with double arrows in Figs. 2(b), 2(f), and 2(j). On-axis harmonic emissions from L1 exhibit the similar behavior to that from S1, i.e., the similar coherence length and the similar minimum position. In the third and fourth rows, spatial distributions of harmonic emissions from S3 and L3 are similar to that from L1, but the emission region along the radial direction is squeezed with multiple branches. Figure 2 displays that the harmonic minimum from different quantum orbits may vary with the spatial point.



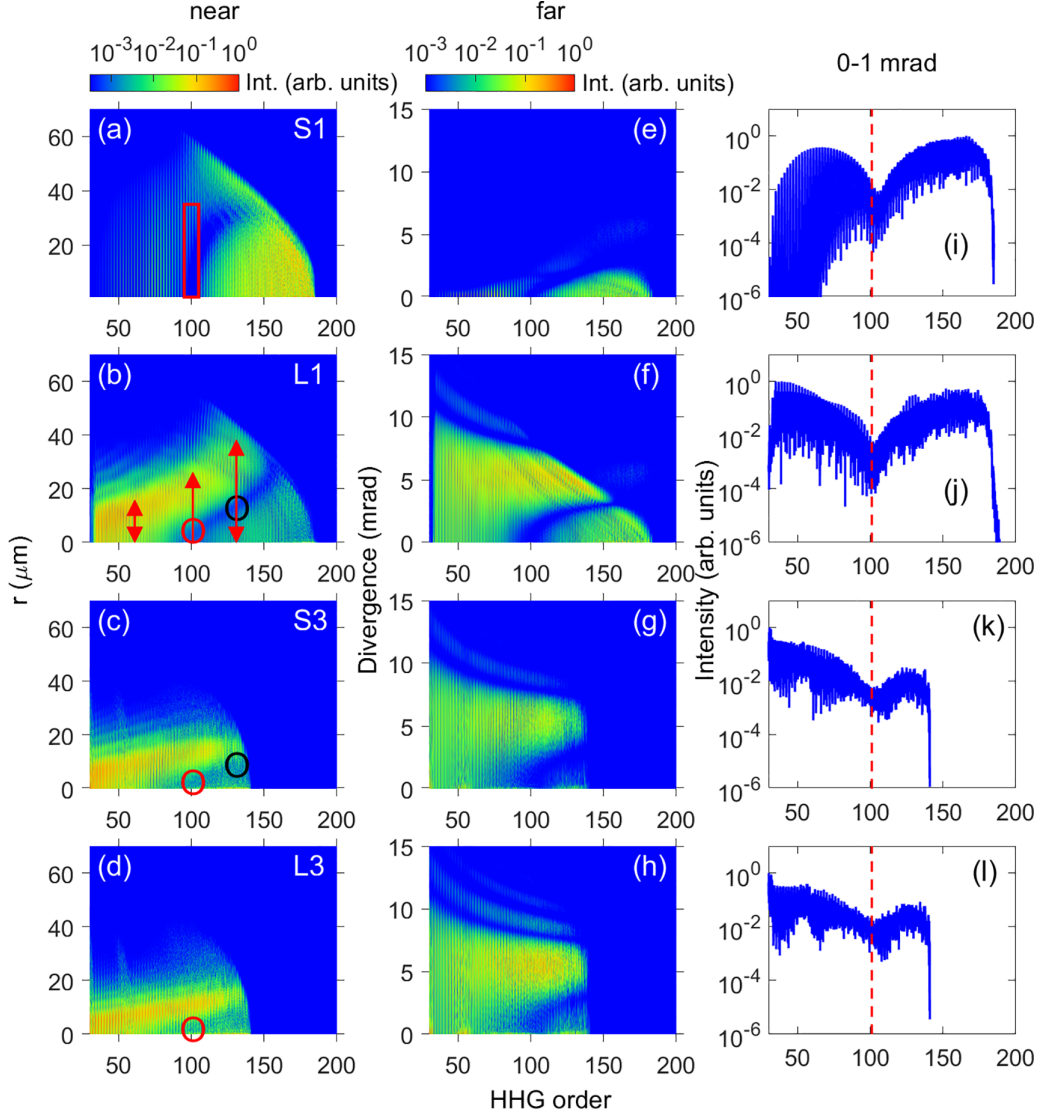


FIG. 2. Harmonic intensity distributions in the near field by (a) S1, (b) L1, (c) S3, and (d) L3. The red square, red arrows, red circles, and black circles are consistent with those in Fig. 3, indicating specific positions on the exit plane of the gas jet. Far-field intensity distributions of high harmonics generated by (e) S1, (f) L1, (g) S3, and (h) L3. The spectra by spatially integrating far-field high harmonics within 0–1 mrad are shown in panels (i)–(l). Red dashed lines indicate the location of H101.

## 2. Calculation of the coherence length of high-order harmonic generation

To analyze the phase matching of HHG, we consider two terms: one is the induced dipole phase in the single-atom response, and the other is the geometric phase of the driving laser. Since the laser intensity and the gas pressure are relatively low in this work, contributions from neutral atom dispersion and plasma to the phase matching can be ignored. For the  $q$ th harmonic, the phase mismatch can be expressed as [67,68]

$$\delta k_q(r, z) = k_q - |q\mathbf{k}_1 + \mathbf{K}|, \quad (18)$$

where  $k_q = q\omega_0/c$ , and  $\mathbf{k}_1$  is the total wave vector of the driving laser, which is explicitly expressed as

$$\mathbf{k}_1(r, z) = k_0\mathbf{e}_z - \nabla\varphi(r, z), \quad (19)$$

where  $\mathbf{e}_z$  is the unit vector along the  $z$  direction,  $\varphi(r, z)$  is the geometric phase of the driving laser, and  $k_0 = \omega_0/c$ . The wave vector  $\mathbf{K}$  describing the spatial dependence of the single-atom dipole phase is given by

$$\mathbf{K}(r, z) = \nabla\varphi_{q,\text{dip}}(r, z). \quad (20)$$

Here  $\varphi_{q,\text{dip}}(r, z)$  is the intrinsic induced dipole phase accumulated by the movement of the electron in the laser field. Its dependence on the laser intensity is written as

$$\varphi_{q,\text{dip}}(r, z) = -\alpha_{i,q}I(r, z), \quad (21)$$

where  $I(r, z)$  is the spatial peak intensity of the driving laser, and the coefficient  $\alpha_{i,q}$  depends on the quantum orbit. The  $\alpha_{i,q}$  values for various quantum orbits have been given in Ref. [69].

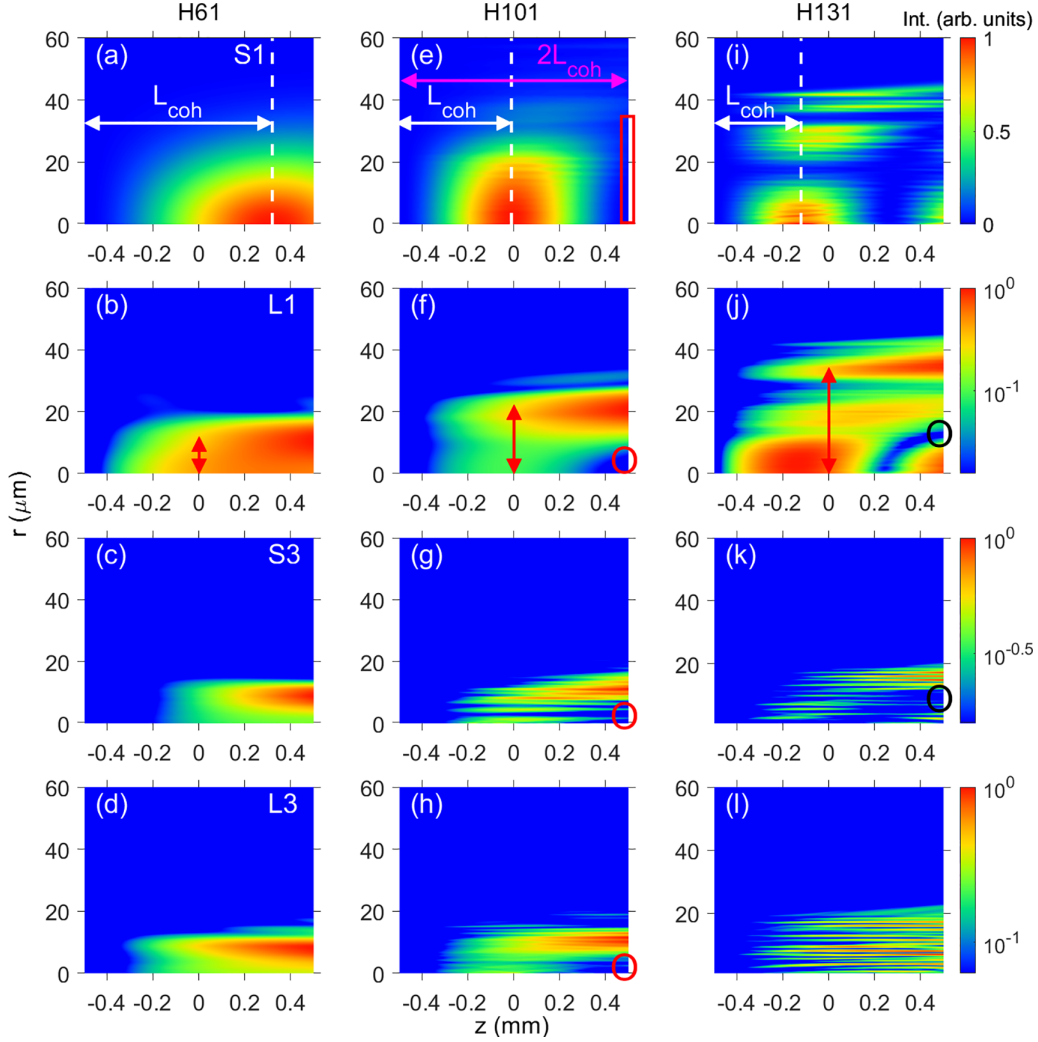


FIG. 3. Spatial evolution of the harmonic field from different quantum orbits inside the gas medium. From the top row to the bottom one, the results are for S1, L1, S3, and L3, respectively. The first, second, and third columns are for H61, H101, and H131, respectively. The white lines with double arrows indicate the harmonic coherence length.

Finally, the coherence length of HHG can be defined as

$$L_{q,\text{coh}}(r, z) = \frac{\pi}{|\delta k_q(r, z)|}. \quad (22)$$

Spatial distributions of the coherence length of HHG for different orders and different quantum orbits are plotted in Fig. 4. The first, second, and third columns are for H61, H101, and H131, respectively. From top row to bottom one, the results are shown for S1, L1, S3, and L3, respectively. In our HHG simulations, the gas jet is located at the focus with the length of 1 mm. Purple lines indicate the location of the gas jet. The coherence length larger than 1 mm is represented by the “white” color.

### 3. Analysis of coherence length maps for different quantum orbits

We then explain the spatial evolution of the harmonic intensity in the gas jet presented in Fig. 3 by using the map of the coherence length. For S1, the phase-matching condition becomes worse with increasing the harmonic order in Figs. 4(a), 4(e), and 4(i), the calculated coherence length at the laser

focus (as indicated in the figures) is 0.82 mm at H61, 0.49 mm at H101, and 0.38 mm at H131. These values agree very well with those identified from numerical simulations in Figs. 3(a), 3(e), and 3(i). We also find that the coherence length is not changed much along the radial direction within the effective HHG generation region for S1. This explains the growth of the harmonic intensity along the propagation distance is similar on axis and off axis in Figs. 3(a), 3(e), and 3(i). With the value of the coherence length, we can determine the harmonic minimum when the following relation is fulfilled:

$$\frac{d}{2L_{\text{coh}}} = n, \quad (23)$$

where  $d$  is the thickness of the gas jet,  $L_{\text{coh}}$  is the coherence length, and  $n \geq 1$  is an integer. For example, in Fig. 3(e), the coherence length is about 0.5 mm, which satisfies Eq. (23) with  $n = 1$ , thus the minimum occurs at H101 in Fig. 2(a). The harmonic minimum could be located both on axis and off axis once the Eq. (23) is satisfied. This equation is also valid for other quantum orbits.

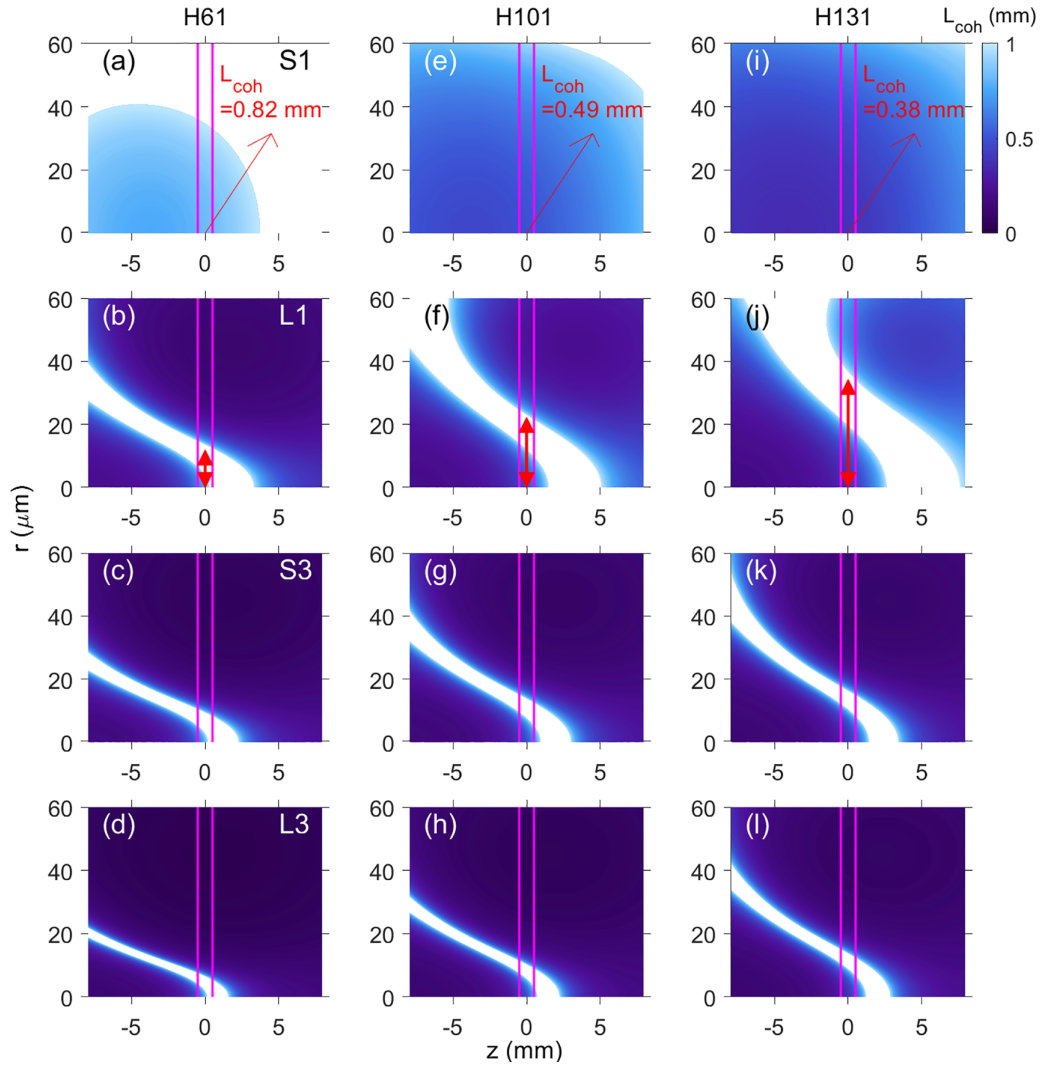


FIG. 4. Maps of the coherence length ( $L_{\text{coh}}$ ) of different harmonics from different quantum orbits. The first, second, third, and fourth rows are for S1, L1, S3, and L3, respectively. The first, second, and third columns show the results for H61, H101, and H131, respectively. The length of the gas jet is labeled by vertical purple lines.

From Eqs. (20) and (21), since the gradient of the laser intensity is zero at the laser focus, the wave vector  $\mathbf{K}$  is zero, i.e., at the laser focus the coherence length is only determined by the geometric phase of the driving laser, which is the same for different quantum orbits. Thus, for L1, S3, and L3, the harmonic minimum also occurs at H101 on axis, labeled by red circles in Figs. 3(f)–3(h), which is similar to that for S1. For L1, the good phase-matching area is gradually moved further off axis with increasing the harmonic order, as labeled by the red lines with double arrows in Figs. 4(b), 4(f), and 4(j), which is quite different from that for S1. This is consistent with the trend that the constant growth area of the harmonic intensity is gradually moved up in Figs. 3(b), 3(f), and 3(j). In Fig. 3(j), there is a minimum formed off axis when  $r < 20 \mu\text{m}$ , as indicated by a black circle. This can be explained that the coherence length is close to 0.5 mm in an off-axis position within  $r < 20 \mu\text{m}$  in Fig. 4(j), thus Eq. (23) is satisfied with  $n = 1$ .

For S3 and L3, the phase-matching condition around the laser focus is similar to that for L1. As shown in Figs. 4(c), 4(g), and 4(k) and Figs. 4(d), 4(h), and 4(l), the favorable phase-matching area becomes narrower along the radial direction compared with that for L1, and is moved up with the harmonic order. Spatial intensity distributions of the harmonic intensity in Figs. 3(c), 3(g), and 3(k) and Figs. 3(d), 3(h), and 3(l) can thus be understood. The origin of the minimum labeled by a black circle off axis in Fig. 3(k) is the same as that in Fig. 3(j). Note that the minimum is absent in Fig. 3(l) because the variation of the coherence length in a limited off-axis area in Fig. 4(l) is so significant that Eq. (23) cannot be fulfilled.

### C. Formation of the harmonic spatial profile in the far field

High-order harmonics exiting from the gas jet propagate in vacuum until the far field. The information of the phase and intensity of the harmonic in the near field determines its

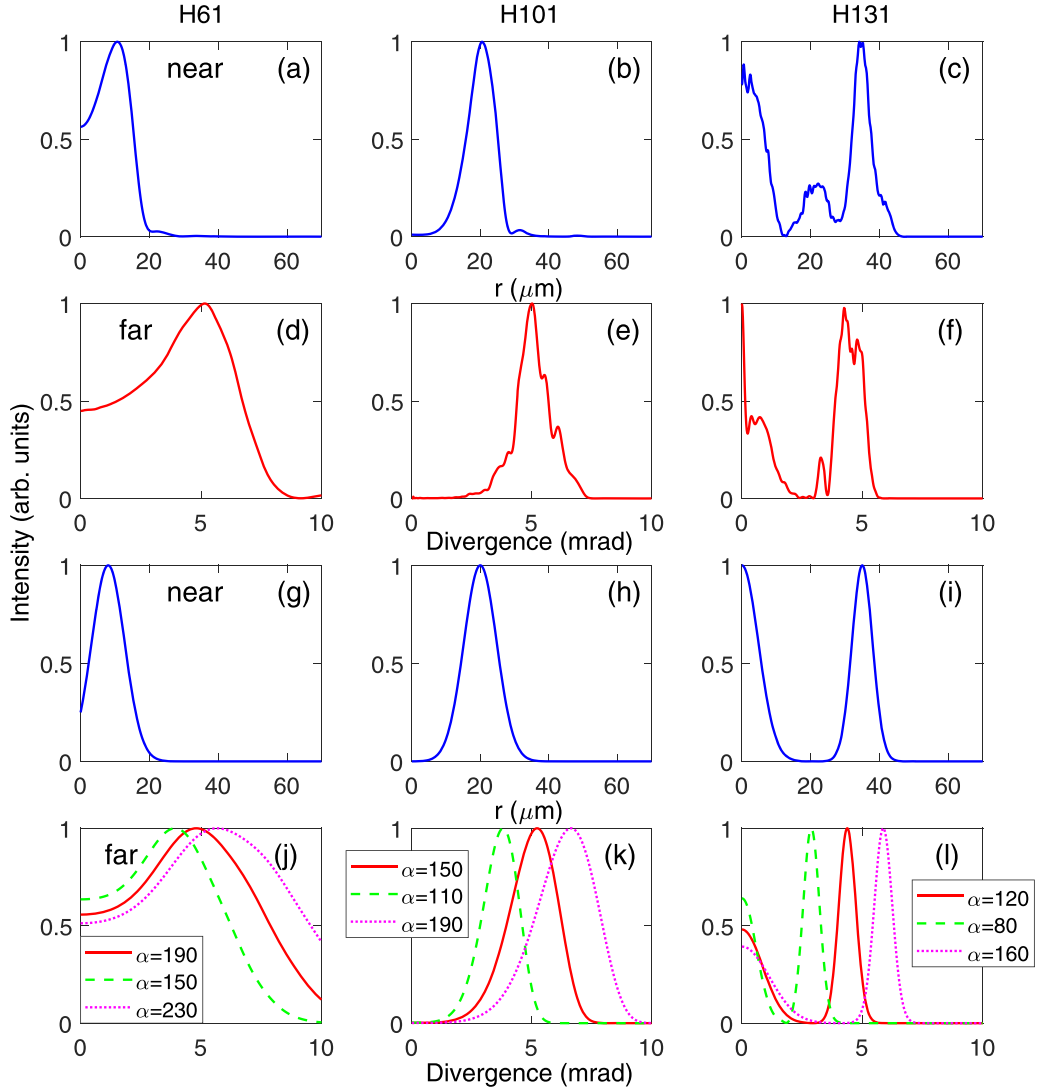


FIG. 5. Near-field intensity profiles of (a) H61, (b) H101, and (c) H131 from rigorous propagation simulations. Similar results in the far field are shown in panels (d)–(f). Here only high harmonics from L1 are considered. Panels (g)–(i) present modeled near-field results. Panels (j)–(l) show the far-field intensity distributions with different  $\alpha$  values. Peak positions in the second row can be well reproduced by red lines in the fourth row. The  $\alpha$  is given in the units of  $10^{-14}$  rad  $W^{-1}$   $cm^2$ .

spatial profile or the minimum structure in the far field. We use high harmonics generated from L1 for illustration. We first show near-field intensity distributions for selected H61, H101, and H131 in Figs. 5(a)–5(c), respectively. And corresponding far-field intensity profiles of those harmonics are plotted in Figs. 5(d)–5(f). These are used to test the model later on.

And then, we adopt a simple model to describe the intensity and phase distributions of the harmonic in the near field. The intensity distribution follows a Gaussian one, and its peak shifts with the harmonic order, as shown in Figs. 5(g)–5(i), respectively. These distributions resemble real ones in the near field very closely. The phase distribution is described as  $\alpha I(r)$ , where  $\alpha$  is the coefficient and  $I(r)$  is the driving laser intensity at the exit plane of the gas jet. The far-field intensity distributions obtained by the model are shown in Figs. 5(j)–5(l). As indicated by the red lines, once the proper  $\alpha$  is chosen, the peak position and the general spatial profile in the far field can be accurately reproduced, compared with

those in Figs. 5(d)–5(f). One can also see that the far-field spatial profile is very sensitive to the  $\alpha$  value. A larger  $\alpha$  leads to a faster phase change along the radial direction in the near field, resulting in a peak position with greater divergence in the far field. From this model, we can conclude that the change of the spatial intensity distribution in the near field is the same as that in the far field, i.e., the peak of the Gaussian-like distribution is shifted further off axis with the harmonic order for L1. This means that the minimum is moved up with the harmonic order, which has been clearly shown in Figs. 2(b) and 2(f).

#### D. Control of the position(s) and the number of the harmonic (multiple) minimum(s)

##### 1. Variation of the laser beam waist

According to Eq. (23), the position(s) and the number of (multiple) minimum(s) could be changed if the coherence



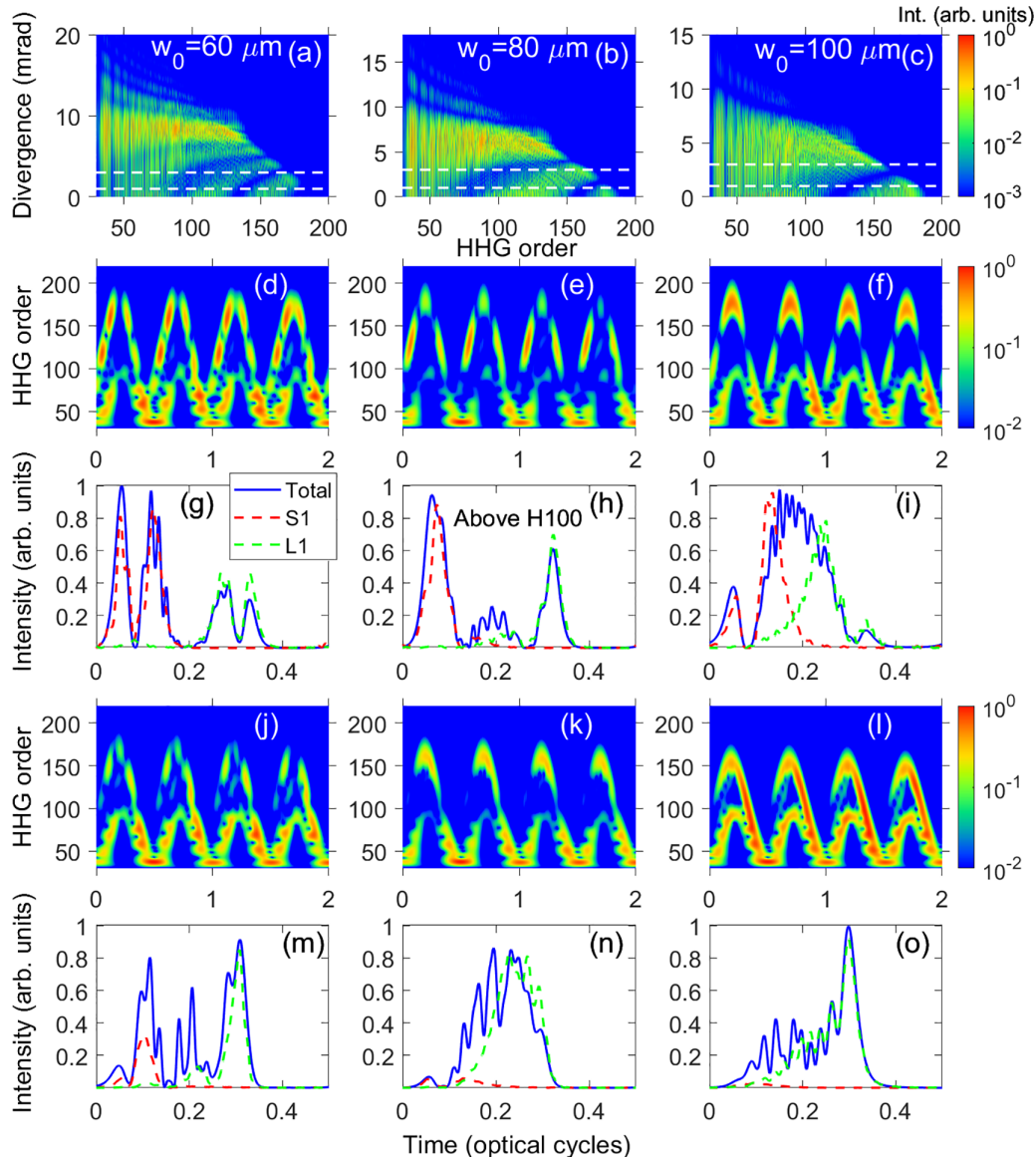


FIG. 6. Far-field intensity distributions of high harmonics generated by the 1600-nm driving laser with different beam waists: (a) 60  $\mu\text{m}$ , (b) 80  $\mu\text{m}$ , and (c) 100  $\mu\text{m}$ . Two spatial positions of 1 and 3 mrad are marked by white dotted lines. Time-frequency analysis of harmonic emissions at 1 mrad are displayed in panels (d)–(f), while the corresponding attosecond pulses in half an optical cycle are presented in panels (g)–(i), which are synthesized by high harmonics above H100. The similar results at 3 mrad are shown in panels (j)–(l) and (m)–(o), respectively.

length of HHG is changed, which can be achieved by varying the macroscopic parameters. First, we vary the beam waist of the driving laser, and other parameters are maintained. Results in the far field are shown in Figs. 6(a)–6(c). When the beam waist is 100  $\mu\text{m}$ , there is only one minimum. If the beam waist is reduced to 80  $\mu\text{m}$ , two minima appear. And there are more minimum structures when the beam waist is decreased to 60  $\mu\text{m}$ , but the minimum structure is not clear in the lower orders. We choose two divergence angles of 1 and 3 mrad to illustrate the features of the time-frequency picture of harmonic emissions and the synthesized attosecond pulses.

At 1 mrad, the time-frequency analysis shows that harmonic emissions from S1 are stronger than that from L1 in Fig. 6(d), with minima clearly appearing around H100 and

H140. The corresponding attosecond pulse by synthesizing the high harmonics above H100 has four peaks in half an optical cycle in Fig. 6(g). Among them, the first two peaks are from S1 while the last two are from L1. We have checked that there is only one peak in each half optical cycle in the attosecond pulse train (APT) of the single-atom response. In Fig. 6(e), the time-frequency harmonic emissions show three divided parts over half an optical cycle above H100, and three major peaks are displayed in the synthesized attosecond pulse in Fig. 6(h). In Fig. 6(f), harmonic emissions in the cutoff region are stronger, which are spectrally separated from emissions of S1 and L1 by the minimum. The resulting attosecond pulse in Fig. 6(i) is separated into two parts, with the first weak one from S1 and the second strong one from merged S1 and L1. At 3 mrad, the position of the minimum changes. From

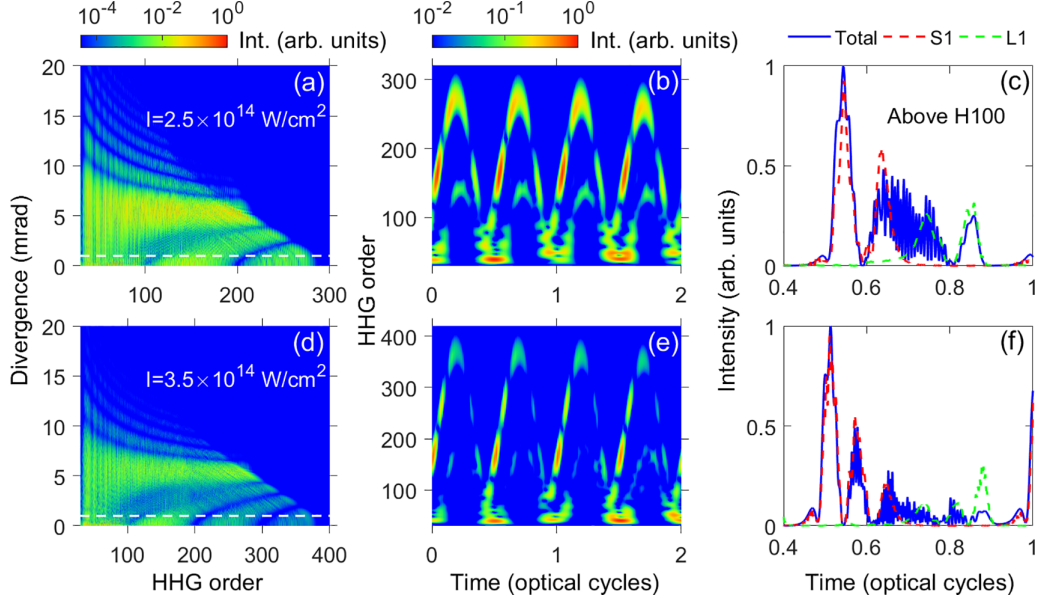


FIG. 7. (a) Intensity distributions of far-field harmonics by the 1600-nm laser with a peak intensity of  $2.5 \times 10^{14}$  W/cm<sup>2</sup> at the focus. Time-frequency picture of harmonic emissions at (b) 1 mrad and corresponding attosecond pulses synthesized by (c) high harmonics above H100. The similar results by changing the intensity as  $3.5 \times 10^{14}$  W/cm<sup>2</sup> are shown in panels (d)–(f), respectively.

Figs. 6(j) and 6(m), there are three separated parts in each half cycle above H100 in the time-frequency picture, corresponding to the first burst (red line) from S1, the second one (blue line) from merged S1 and L1, and the third one (green line) from L1 in the attosecond pulse. There is no minimum in Figs. 6(k) and 6(l). Thus the main burst in the attosecond pulse is from L1 (green lines) in Figs. 6(n) and 6(o).

Therefore, the position(s) and the number of (multiple) minimum(s) in the far field can be adjusted by varying the laser beam waist. In the time domain, this can be used to shape the profile of the attosecond pulse and change the width of the emission burst in the APT. Note that the minimum in the HHG spectrum cannot be created if the laser beam waist is set too small.

## 2. Variation of the laser intensity

We then check how the minimum structure in the HHG spectrum is influenced by the laser intensity. We change the intensity to  $2.5 \times 10^{14}$  W/cm<sup>2</sup> and fix other parameters. The resulting harmonic intensity distribution in the far field is shown in Fig. 7(a), and the time-frequency analysis of harmonic emissions and the profile of the attosecond pulse (synthesized by high harmonics above H100) at 1 mrad are shown in Figs. 7(b) and 7(c), respectively. The similar results for the intensity of  $3.5 \times 10^{14}$  W/cm<sup>2</sup> are shown in Figs. 7(d)–7(f). Comparing Figs. 1(b), 7(a), and 7(d), the number of (multiple) minimum(s) is increased by increasing the laser intensity, but the minimum at the lower order does not move; for example, the minimum at H101 on the axis. The increase in the number of multiple minima with the laser intensity can also be seen in the time-frequency harmonics emissions in Figs. 7(b) and 7(e). Consequently, in the APT, there is an increase in the number of emission peaks within

half an optical period, effectively reducing the width of each emission burst, see Figs. 7(c) and 7(f).

## 3. Scaling relations with the laser wavelength

Can the similar minimum structure in the HHG spectrum emerge by changing the laser wavelength? It is desirable if the HHG spectrum with the minimum can be scalable. For simplicity, we derive a scaling relation by considering the harmonic coherence length along the axis. According to Eq. (18), the phase mismatch at the laser focus can be expressed as

$$\begin{aligned} \delta k_q &= k_q - |q\mathbf{k}_1 + \mathbf{K}| = q\omega_0/c - \left( q\omega_0/c - \frac{q\lambda_0}{\pi w_0^2} \right) \\ &= \frac{q\lambda_0}{\pi w_0^2}, \end{aligned} \quad (24)$$

where  $w_0$  is the laser beam waist,  $\lambda_0$  is the laser wavelength, and  $q$  is the harmonic order. Note that  $\mathbf{K}$  is zero at the laser focus. To maintain the same phase mismatch (or the coherence length), we can obtain the following scaling relations:

$$\begin{aligned} \lambda_0 &\rightarrow \eta\lambda_0, \\ w_0 &\rightarrow \eta w_0, \\ q &\rightarrow \eta q. \end{aligned} \quad (25)$$

Here  $\eta$  is a scaling parameter.

To check the scaling relations above, we show spatial harmonic emissions in the far field by using a 1200-nm laser in Figs. 8(a)–8(c). Three beam waists of 50, 55, and 63  $\mu\text{m}$  are chosen to ensure that the harmonic minimum can be generated. The gas jet with the length of 1 mm is put at the focus. The intensity of the driving beam at the laser focus is fixed at  $1.5 \times 10^{14}$  W/cm<sup>2</sup>. The total pulse duration is 30 optical cycles, and the CEP is zero. According to the scaling relations in Eq. (25), we choose the beam waists of 66.7,

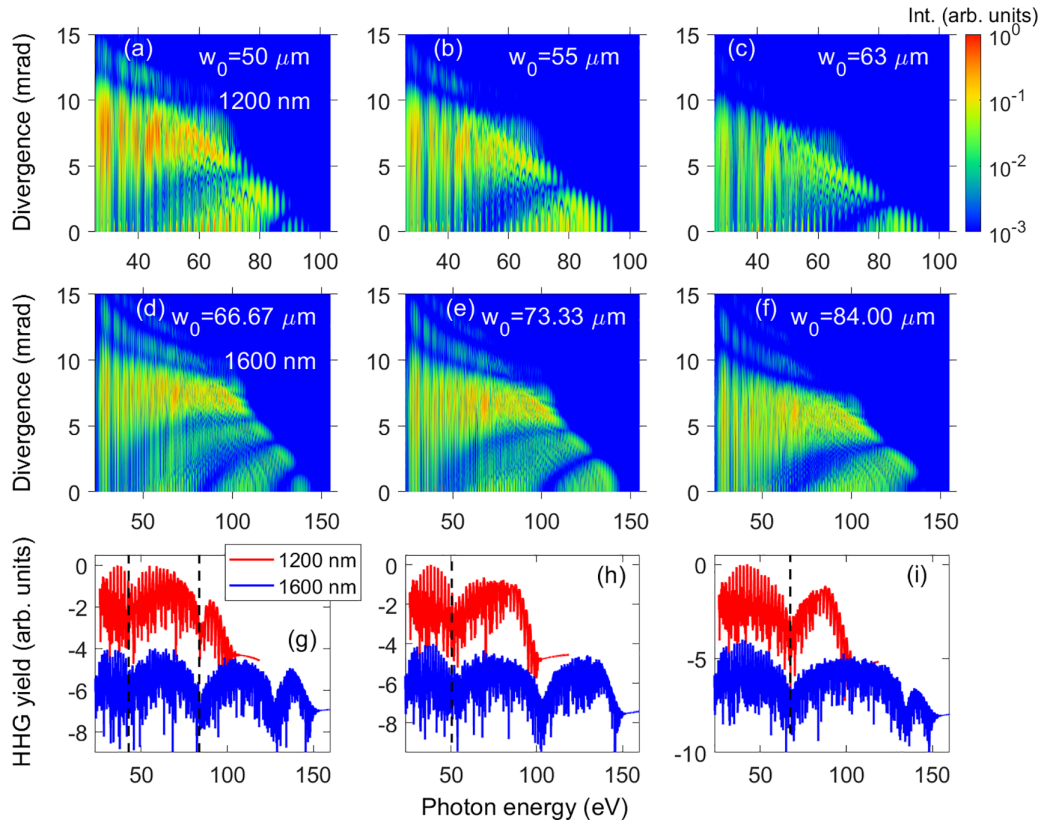


FIG. 8. Intensity distributions of high harmonics in the far field generated by the 1200-nm laser with different beam waists: (a)  $50 \mu\text{m}$ , (b)  $55 \mu\text{m}$ , and (c)  $63 \mu\text{m}$ . Similar results by the 1600-nm laser are shown in panels (d)–(f) as the beam waists are chosen according to the scaling relations in Eq. (25). For comparison, harmonic spectra of two wavelengths on the axis are plotted together in panels (g)–(i), in which black dotted line indicates the location of the minimum.

73.3, and  $84.0 \mu\text{m}$  for the 1600-nm laser. Results are shown in Figs. 8(d)–8(f). One can see that the number of (multiple) minimum(s) decreases as the laser beam waist increases. This trend is the same for both wavelengths. We compare the harmonic spectra on the axis at different wavelengths in Figs. 8(g)–8(i). Note that the horizontal axis in these figures is expressed with the photon energy for easy comparison, and the black dotted line indicates the minimum. It can be seen that the minimum appears in the same position at different wavelengths. Thus the scaling relation of the harmonic order is confirmed, which shows that the photon energy of the minimum is not varied with the laser wavelength. Resemblance of spatial harmonic emissions at two different wavelengths verifies the validity of the scaling relations in Eq. (25) even though rigorous propagation effects in the gas medium has been fully taken into account.

Simulations in this section show that the position of the minimum in the HHG spectrum can be easily shifted. This is one of advantages of our method compared with the conventional method, in which the fixed minimum is generated in the HHG spectrum of an atom target, relating to the minimum in the photoionization cross section of the same target.

The minimum in the HHG spectrum can also be modified by varying the gas pressure. For example, we have observed that the position of the minimum in Fig. 1 shifts towards higher harmonics if the gas pressure is increased to 30 or 50 torr, which can be explained by the similar

analysis of the phase mismatch. Specifically, the positive phase mismatch due to neutral atom dispersion, increased with the gas pressure, should be compensated by that due to the geometric phase of the driving laser though increasing the harmonic order. However, the phase-matching conditions of high harmonics are very sensitive to the gas pressure. It requires considerable efforts to identify the proper conditions for creating the minimum in the HHG spectrum under the high-pressure (several hundred torr) condition, or more generally under the extreme condition of high pressure and high intensity. Meanwhile, the effect of self-absorption of high harmonics by the gas medium should be carefully considered. This is a topic worth investigating in the future.

Note that we employ a Gaussian beam as the driving laser beam in this work. Alternatively, a Laguerre-Gaussian beam carrying the orbital angular momentum may be adopted [53]. Further detailed studies are required.

#### IV. CONCLUSIONS

In summary, we demonstrated through rigorous simulations that the minimum in the HHG spectrum can be created and tuned by varying the macroscopic parameters properly with a single-color long-wavelength laser only. We first showed that a curved minimum structure exists in the harmonic intensity distributions both in the near field and in the

far field when the gas jet is located at the laser focus and the driving laser has a relatively big beam waist. The minimum in the HHG spectrum thus can be spectrally shifted with the spatial position. It is worth noting that there is no minimum in the single-atom HHG spectrum of the Ne atom. We revealed that the position of the minimum is fixed along the radial direction for the short orbit of the first return (S1), and it is shifted towards higher orders as the radial distance (or the divergence angle) increases for the long orbit of the first return (L1), the short orbit of the third return (S3), and the long orbit of the third return (L3). We examined the spatial evolution of the harmonic field inside the gas medium from different quantum orbits. It shows that the behaviors of the field growth for S1 are quite different from that for L1, S3, and L3. Such differences among quantum orbits can be well explained by the calculated maps of the coherence length. We also gave a formula to predict the spectral position of the minimum in terms of the coherence length. We then proposed a simple model to describe the near-field harmonic and explained the formation of the harmonic spatial profile in the far field. We showed that the position(s) and the number of (multiple) minimum(s) can be tuned by varying the beam waist and the intensity of the driving laser. A smaller waist and a larger intensity are beneficial for increasing the number of multiple minima, which can also be used to shape the temporal profile of the attosecond

pulse in the attosecond pulse train and to reduce the width of emission burst. Finally, we derived the scaling relations with the laser wavelength to maintain the spectral position of the minimum and the phase-matching condition. Since the method in this study is simple and robust, it can be easily applied to shape the attosecond pulse and modify the spectral structure, making the HHG light being a useful light source for various applications.

As we know, the phase-matching conditions of the HHG are very sensitive to the macroscopic parameters, and it is impossible to scan all macroscopic parameters in a single experiment. Without the guidance of this work, the experimentalists hardly identify the macroscopic condition for creating and controlling the minimum in the HHG spectrum. Thus our results and the established rules (or relations) are useful to the HHG community.

#### ACKNOWLEDGMENTS

This work was supported by National Natural Science Foundation of China (NSFC) under Grant No. 12274230 and Funding of Nanjing University of Science and Technology (NJUST) under Grant No. TSXK2022D005. We sincerely thank Dr. Hui Wei for useful discussions about the QO model.

- 
- [1] A. McPherson, G. Gibson, H. Jara, U. Johann, T. S. Luk, I. A. McIntyre, K. Boyer, and C. K. Rhodes, *J. Opt. Soc. Am. B* **4**, 595 (1987).
- [2] M. Ferray, A. L'Huillier, X. F. Li *et al.*, *J. Phys. B: At., Mol. Opt. Phys.* **21**, L31 (1988).
- [3] P. Salières, A. L'Huillier, Ph. Antoine, and M. Lewenstein, *Adv. At. Mol. Opt. Phys.* **41**, 83 (1999).
- [4] C. Winterfeldt, C. Spielmann, and G. Gerber, *Rev. Mod. Phys.* **80**, 117 (2008).
- [5] F. Krausz and M. Ivanov, *Rev. Mod. Phys.* **81**, 163 (2009).
- [6] T. Brabec and F. Krausz, *Rev. Mod. Phys.* **72**, 545 (2000).
- [7] L. Y. Peng, W. C. Jiang, J. W. Geng, W. H. Xiong, and Q. Gong, *Phys. Rep.* **575**, 1 (2015).
- [8] T. Popmintchev, M. C. Chen, D. Popmintchev, P. Arpin, S. Brown, S. Ališauskas, G. Andriukaitis, T. Balčiūnas, O. D. Mücke, A. Pugzlys, A. Baltuška, B. Shim, S. E. Schrauth, A. Gaeta, C. Hernández-García, L. Plaja, A. Becker, A. Jaron-Becker, M. M. Murnane, and H. C. Kapteyn, *Science* **336**, 1287 (2012).
- [9] J. Seres, E. Seres, A. J. Verhoef, G. Tempea, C. Strelci, P. Wobrowschek, V. Yakovlev, A. Scrinzi, C. Spielmann, and F. Krausz, *Nature (London)* **433**, 596 (2005).
- [10] B. Xue, Y. Tamaru, Y. Fu, H. Yuan, P. Lan, O. D. Mücke, A. Suda, K. Midorikawa, and E. J. Takahashi, *Ultrafast Sci.* **2021**, 9828026 (2021).
- [11] P. Ye, L. G. Oldal, T. Csizmadia, Z. Filus, T. Grósz, P. Jójárt, I. Seres, Z. Bengery, B. Gilicze, S. Kahaly, K. Varjú, and B. Major, *Ultrafast Sci.* **2022**, 9823783 (2022).
- [12] P. M. Paul, E. S. Toma, P. Breger, G. Mullot, F. Augé, P. Balcou, H. G. Muller, and P. Agostini, *Science* **292**, 1689 (2001).
- [13] M. Hentschel, R. Kienberger, C. Spielmann, G. A. Reider, N. Milosevic, T. Brabec, P. Corkum, U. Heinzmann, M. Drescher, and F. Krausz, *Nature (London)* **414**, 509 (2001).
- [14] M. Asaki, C. P. Huang, D. Garvey, J. Zhou, H. C. Kapteyn, and M. M. Murnane, *Opt. Lett.* **18**, 977 (1993).
- [15] R. Kienberger, M. Hentschel, M. Uiberacker, Ch. Spielmann, M. Kitzler, A. Scrinzi, M. Wieland, Th. Westerwalbesloh, U. Kleineberg, U. Heinzmann, M. Drescher, and F. Krausz, *Science* **297**, 1144 (2002).
- [16] M. Uiberacker, Th. Uphues, M. Schultze, A. J. Verhoef, V. Yakovlev, M. F. Kling, J. Rauschenberger, N. M. Kabachnik, H. Schröder, M. Lezius, K. L. Kompa, H.-G. Müller, M. J. J. Vrakking, S. Hendel, U. Kleineberg, U. Heinzmann, M. Drescher, and F. Krausz, *Nature (London)* **446**, 627 (2007).
- [17] Y. Huang, J. Zhao, Z. Shu, Y. Zhu, J. Liu, W. Dong, X. Wang, Z. Lü, D. Zhang, J. Yuan, J. Chen, and Z. Zhao, *Ultrafast Sci.* **2021**, 9837107 (2021).
- [18] E. Goulielmakis, Z. H. Loh, A. Wirth *et al.*, *Nature (London)* **466**, 739 (2010).
- [19] M. Schultze, E. M. Bothschafter, A. Sommer *et al.*, *Nature (London)* **493**, 75 (2013).
- [20] F. Calegari, D. Ayuso, A. Trabattoni *et al.*, *Science* **346**, 336 (2014).
- [21] U. S. Sainadh, H. Xu, X. Wang *et al.*, *Nature (London)* **568**, 75 (2019).
- [22] O. Kneller, D. Azoury, Y. Federman *et al.*, *Nat. Photonics* **16**, 304 (2022).
- [23] J. Itatani, J. Levesque, D. Zeidler, H. Niikura, H. Pápin, J. C. Kieffer, P. B. Corkum, and D. M. Villeneuve, *Nature (London)* **432**, 867 (2004).
- [24] Y. Pertot, C. Schmidt, M. Matthews, A. Chauvet, M. Huppert, V.



- Svoboda, A. von Conta, A. Tehlar, D. Baykusheva, J.-P. Wolf, and H. J. Wörner, *Science* **355**, 264 (2017).
- [25] J. Miao, T. Ishikawa, I. K. Robinson, and M. M. Murnane, *Science* **348**, 530 (2015).
- [26] A. Ozawa, J. Rauschenberger, C. Gohle, M. Herrmann, D. R. Walker, V. Pervak, A. Fernandez, R. Graf, A. Apolonski, R. Holzwarth, F. Krausz, T. W. Hänsch, and T. Udem, *Phys. Rev. Lett.* **100**, 253901 (2008).
- [27] B. Zhang, D. F. Gardner, M. H. Seaberg, E. R. Shanblatt, C. L. Porter, R. Karl, C. A. Mancuso, H. C. Kapteyn, M. M. Murnane, and D. E. Adams, *Opt. Express* **24**, 18745 (2016).
- [28] S. L. Cousin, N. Di Palo, B. Buades, S. M. Teichmann, M. Reduzzi, M. Devetta, A. Kheifets, G. Sansone, and J. Biegert, *Phys. Rev. X* **7**, 041030 (2017).
- [29] C. Jin, S. J. Wang, X. Zhao, S. F. Zhao, and C. D. Lin, *Phys. Rev. A* **101**, 013429 (2020).
- [30] C. Jin, S. J. Wang, S. F. Zhao, A. T. Le, and C. D. Lin, *Phys. Rev. A* **102**, 013108 (2020).
- [31] S. B. Schoun, R. Chirla, J. Wheeler, C. Roedig, P. Agostini, L. F. DiMauro, K. J. Schafer, and M. B. Gaarde, *Phys. Rev. Lett.* **112**, 153001 (2014).
- [32] X. Y. Li, J. X. Han, L. W. Liu, X. L. Wang, G. L. Wang, and C. Jin, *Phys. Rev. A* **109**, 023103 (2024).
- [33] Y. Fu, B. C. Wan, K. Wan, X. Y. Tang, B. C. Li, Z. M. Yin, J. X. Han, C. D. Lin, and C. Jin, *Proc. Natl. Acad. Sci. USA* **121**, e2307836121 (2024).
- [34] A. D. Shiner, B. E. Schmidt, C. Trallero-Herrero, H. J. Wörner, S. Patchkovskii, P. B. Corkum, J.-C. Kieffer, F. Légaré, and D. M. Villeneuve, *Nat. Phys.* **7**, 464 (2011).
- [35] H. J. Wörner, H. Niikura, J. B. Bertrand, P. B. Corkum, and D. M. Villeneuve, *Phys. Rev. Lett.* **102**, 103901 (2009).
- [36] S. Minemoto, T. Umegaki, Y. Oguchi, T. Morishita, A. T. Le, S. Watanabe, and H. Sakai, *Phys. Rev. A* **78**, 061402(R) (2008).
- [37] E. J. Takahashi, T. Kanai, Y. Nabekawa, and K. Midorikawa, *Appl. Phys. Lett.* **93**, 041111 (2008).
- [38] P. Colosimo, G. Doumy, C. I. Bлага, J. Wheeler, C. Hauri, F. Catoire, J. Tate, R. Chirla, A. M. March, G. G. Paulus, H. G. Muller, P. Agostini, and L. F. Dimauuro, *Nat. Phys.* **4**, 386 (2008).
- [39] J. P. Farrell, L. S. Spector, B. K. McFarland, P. H. Bucksbaum, M. Gühr, M. B. Gaarde, and K. J. Schafer, *Phys. Rev. A* **83**, 023420 (2011).
- [40] J. Higuët, H. Ruf, N. Thiré, R. Cireasa, E. Constant, E. Cormier, D. Descamps, E. Mével, S. Petit, B. Pons, Y. Mairesse, and B. Fabre, *Phys. Rev. A* **83**, 053401 (2011).
- [41] C. Jin, H. J. Wörner, V. Tosa, A. T. Le, J. B. Bertrand, R. R. Lucchese, P. B. Corkum, D. M. Villeneuve, and C. D. Lin, *J. Phys. B: At., Mol. Opt. Phys.* **44**, 095601 (2011).
- [42] T. Kanai, S. Minemoto, and H. Sakai, *Nature (London)* **435**, 470 (2005).
- [43] C. Vozzi, F. Calegari, E. Benedetti, J.-P. Caumes, G. Sansone, S. Stagira, M. Nisoli, R. Torres, E. Heesel, N. Kajumba, J. P. Marangos, C. Altucci, and R. Velotta, *Phys. Rev. Lett.* **95**, 153902 (2005).
- [44] A. Rupenyan, P. M. Kraus, J. Schneider, and H. J. Wörner, *Phys. Rev. A* **87**, 031401(R) (2013).
- [45] A. Rupenyan, P. M. Kraus, J. Schneider, and H. J. Wörner, *Phys. Rev. A* **87**, 033409 (2013).
- [46] M. Lein, N. Hay, R. Velotta, J. P. Marangos, and P. L. Knight, *Phys. Rev. Lett.* **88**, 183903 (2002).
- [47] W. Boutu, S. Haessler, H. Merdji, P. Breger, G. Waters, M. Stankiewicz, L. J. Frasinski, R. Taieb, J. Caillat, A. Maquet, P. Monchicourt, B. Carre, and P. Salieres, *Nat. Phys.* **4**, 545 (2008).
- [48] O. Smirnova, Y. Mairesse, S. Patchkovskii, N. Dudovich, D. Villeneuve, P. Corkum, and M. Yu. Ivanov, *Nature (London)* **460**, 972 (2009).
- [49] H. J. Wörner, J. B. Bertrand, P. Hockett, P. B. Corkum, and D. M. Villeneuve, *Phys. Rev. Lett.* **104**, 205702 (2010).
- [50] C. Vozzi, M. Negro, F. Calegari, G. Sansone, M. Nisoli, S. De Silvestri, and S. Stagira, *Nat. Phys.* **7**, 822 (2011).
- [51] H. Yun, K.-M. Lee, J. H. Sung, K. T. Kim, H. T. Kim, and C. H. Nam, *Phys. Rev. Lett.* **114**, 153901 (2015).
- [52] C. Jin and C. D. Lin, *Photonics Res.* **6**, 434 (2018).
- [53] C. Jin, B. C. Li, K. Wang, C. H. Xu, X. Y. Tang, C. Yu, and C. D. Lin, *Phys. Rev. A* **102**, 033113 (2020).
- [54] C. Jin, A. T. Le, and C. D. Lin, *Phys. Rev. A* **79**, 053413 (2009).
- [55] M. Lewenstein, Ph. Balcou, M. Yu. Ivanov, A. L'Huillier, and P. B. Corkum, *Phys. Rev. A* **49**, 2117 (1994).
- [56] A. T. Le, H. Wei, C. Jin, and C. D. Lin, *J. Phys. B: At., Mol. Opt. Phys.* **49**, 053001 (2016).
- [57] T. Morishita, A. T. Le, Z. Chen, and C. D. Lin, *Phys. Rev. Lett.* **100**, 013903 (2008).
- [58] A. T. Le, R. R. Lucchese, S. Tonzani, T. Morishita, and C. D. Lin, *Phys. Rev. A* **80**, 013401 (2009).
- [59] P. Salières, B. Carré, L. Le Déroff, F. Grasbon, G. G. Paulus, H. Walther, R. Kopold, W. Becker, D. B. Milošević, A. Sanpera, and M. Lewenstein, *Science* **292**, 902 (2001).
- [60] D. B. Milošević and W. Becker, *Phys. Rev. A* **66**, 063417 (2002).
- [61] G. Sansone, C. Vozzi, S. Stagira, and M. Nisoli, *Phys. Rev. A* **70**, 013411 (2004).
- [62] D. J. Hoffmann, C. Hutchison, A. Zaïr, and J. P. Marangos, *Phys. Rev. A* **89**, 023423 (2014).
- [63] C. D. Lin, A. T. Le, C. Jin, and H. Wei, *Attosecond and Strong-Field Physics: Principles and Applications* (Cambridge University Press, Cambridge, 2018), pp. 209–232.
- [64] E. Priori, G. Cerullo, M. Nisoli, S. Stagira, S. De Silvestri, P. Villoresi, L. Poletto, P. Ceccherini, C. Altucci, R. Bruzzese, and C. de Lisio, *Phys. Rev. A* **61**, 063801 (2000).
- [65] X. M. Tong and C. D. Lin, *J. Phys. B: At., Mol. Opt. Phys.* **38**, 2593 (2005).
- [66] C. Jin, G. L. Wang, A. T. Le, and C. D. Lin, *Sci. Rep.* **4**, 7067 (2014).
- [67] P. Balcou, P. Salières, A. L'Huillier, and M. Lewenstein, *Phys. Rev. A* **55**, 3204 (1997).
- [68] L. E. Chipperfield, P. L. Knight, J. W. G. Tisch, and J. P. Marangos, *Opt. Commun.* **264**, 494 (2006).
- [69] Z. M. Yin, X. Y. Tang, X. H. Li, B. Y. Wang, J. X. Han, C. D. Lin, and C. Jin, *Phys. Rev. A* **107**, 013114 (2023).